Densification Behavior of Tungsten Heavy Alloy Based on Master Sintering Curve Concept

S.J. PARK, J.M. MARTIN, J.F. GUO, J.L. JOHNSON, and RANDALL M. GERMAN

The master sintering curve (MSC) theory is modified by substituting the densification ratio (Φ) for the densification parameter (Ψ) to identify regions where shrinkage occurs by a similar combination of sintering mechanisms. The modified MSC theory is used to analyze the results of dilatometry experiments conducted with W-Ni-Fe heavy alloys, in which a phase change occurs during sintering. Apparent activation energies for sintering in three regions (solid state, transition, and liquid phase) are calculated. These activation energies are compared with experimental values for diffusion and other mass-transport phenomena to identify the dominant mechanisms in each region. A series of master sinter curves for varying W contents are developed into a master sintering surface that includes tungsten content and integral work.

I. INTRODUCTION

TUNGSTEN heavy alloys (WHAs) are used for a number of applications, including radiation shields, counterweights, electrical contacts, gyroscopic components, vibration dampeners, and kinetic energy penetrators.[1] The most common compositions consist of W along with some combination of Ni, Fe, or Cu, although small amounts of other transition metals are sometimes added. The WHAs can be readily processed to near theoretical density by sintering at temperatures at which a liquid phase is present. However, significant densification occurs by solid-state sintering during heating prior to liquid-phase formation.[2–5] The Ni and Fe additions, in particular, enhance the solid-state sintering of W.[6] Changes in the dominant sintering mechanism at different stages of the sintering cycle complicate analysis of densification behavior. In this article, the master sintering curve (MSC) concept is modified to analyze densification during heating of W-Ni-Fe heavy alloys with W contents ranging from 83 to 93 wt pct.

II. MSC THEORY

During solid-state and liquid-phase sintering of most materials, diffusion plays the primary role in densification,[7] although grain rearrangement can also be very important in liquid-phase sintering.[8] In solid-state sintering, either grain boundary or volume diffusion is the dominant densification mechanism. Surface diffusion is active with small powders, but does not contribute to densification. The following multiple mechanism model provides a means to predict densification behavior:[9]

$$\frac{1}{3\rho}\frac{d\rho}{dt} = \frac{\gamma_{sv}\Omega}{\mathrm{k}T}\left(\frac{\Gamma_v D_v}{G^3} + \frac{\Gamma_b \delta_b D_b}{G^4}\right) \quad [1]$$

where ρ is the relative density, t is the time, γ_{sv} is the solid-vapor surface energy, Ω is the atomic volume, k is Boltzmann's constant, T is the absolute temperature, Γ is a density-dependent function, D is a diffusivity, G is the grain size, δ_b is the width of the grain boundary, the subscript v stands for volume diffusion, and the subscript b stands for grain boundary diffusion. Taking into account the exponential dependence of the diffusivities with temperature, the previous equation can be rewritten as

$$\frac{1}{3\rho}\frac{d\rho}{dt} = \frac{\gamma_{sv}\Omega}{\mathrm{k}T}\left[\frac{\Gamma_v D_{v0}}{G^3}\exp\left(-\frac{Q_v}{\mathrm{R}T}\right) + \frac{\Gamma_b \delta_b D_{b0}}{G^4}\exp\left(-\frac{Q_b}{\mathrm{R}T}\right)\right] \quad [2]$$

where R is the universal gas constant, D_{v0} and D_{b0} are the pre-exponential factors, and Q_v and Q_b are the activation energies for volume and grain boundary diffusion, respectively. It is noteworthy to mention that in all crystalline materials, $Q_b < Q_v$, because grain boundaries are high diffusivity paths.

When volume diffusion is the dominant sintering mechanism, Eq. [2] can be simplified as

$$\frac{1}{3\rho}\frac{d\rho}{dt} = \frac{\gamma_{sv}\Omega}{\mathrm{k}}\frac{\Gamma_v D_{v0}}{G^3}\frac{1}{T}\exp\left(-\frac{Q_v}{\mathrm{R}T}\right) \quad [3]$$

Similarly, when grain boundary diffusion is the dominant sintering mechanism, Eq. [2] can be simplified as

$$\frac{1}{3\rho}\frac{d\rho}{dt} = \frac{\gamma_{sv}\Omega}{\mathrm{k}}\frac{\Gamma_b \delta_b D_{b0}}{G^4}\frac{1}{T}\exp\left(-\frac{Q_b}{\mathrm{R}T}\right) \quad [4]$$

If the dominant densification mechanism is not known, Eq. [3] or [4] can be used to determine experimentally an apparent activation energy for sintering (Q) using the shrinkage-rate data obtained in either isothermal experiments at different temperatures or constant-heating-rate experiments at different heating rates. This apparent activation

S.J. PARK, Associate Research Professor, and RANDALL M. GERMAN, Director and CAVS Chair Professor of Mechanical Engineering, are with the Center for Advanced Vehicular Systems, Mississippi State University, Mississippi State, MS 39762. Contact e-mail: sjpark@cavs.msstate.edu J.M. MARTIN, Staff Researcher, is with the Centro de Estudios e Investigaciones Técnicas de Guipúzcoa (CEIT) and TECNUN, 20018 San Sebastián, Spain. J.F. GUO, Graduate Student, is with the Center for Innovative Sintered Products, CISP Lab, The Pennsylvania State University, University Park, PA 16802. J.L. JOHNSON, Staff Engineer, is with Breakthrough Technology, Kennametal Inc., Latrobe, PA 15650.

Manuscript submitted August 29, 2005.

energy for sintering (Q) can be compared with activation energies for diffusion processes (either Q_v or Q_b) determined by other methods to identify the dominant densification mechanism.[10–14]

If the apparent activation energy for sintering (Q) does not match any diffusion activation energy between the margins of experimental error, the contribution to shrinkage from both mechanisms could be significant, so no one of them can be neglected. This apparent activation energy (Q) results from assuming one common activation energy in Eq. [2] for both participating densification mechanisms:

$$\frac{1}{3\rho}\frac{d\rho}{dt} = \frac{\gamma_{sv}\Omega}{\mathrm{k}}\left(\frac{\Gamma_v D_{v0}}{G^3} + \frac{\Gamma_b \delta_b D_{b0}}{G^4}\right)\frac{1}{T}\exp\left(-\frac{Q}{\mathrm{R}T}\right) \quad [5]$$

Comparing Eq. [2] with Eq. [5], it is evident that

$$\exp\left(-\frac{Q}{\mathrm{R}T}\right) = \frac{\dfrac{\Gamma_v D_{v0}}{G^3}}{\dfrac{\Gamma_v D_{v0}}{G^3} + \dfrac{\Gamma_b \delta_b D_{b0}}{G^4}}\exp\left(-\frac{Q_v}{\mathrm{R}T}\right) + \frac{\dfrac{\Gamma_b \delta_b D_{b0}}{G^4}}{\dfrac{\Gamma_v D_{v0}}{G^3} + \dfrac{\Gamma_b \delta_b D_{b0}}{G^4}}\exp\left(-\frac{Q_b}{\mathrm{R}T}\right) \quad [6]$$

This expression shows that the apparent activation energy from sintering (Q) is always between Q_b and Q_v, that is, $Q_b < Q < Q_v$. Then, Q can be compared with possible values of Q_v and Q_b in order to detect which diffusion sintering mechanisms are acting simultaneously. Additionally, Eq. [6] implies that Q is one single constant when the proportional contribution of both involved sintering mechanisms is constant during the entire range of temperatures under study.

Eq. [5] can be further modified as

$$\frac{1}{3\rho}\frac{d\rho}{dt} = \frac{\gamma\Omega\Gamma D_0}{\mathrm{k}G^m}\frac{1}{T}\exp\left(-\frac{Q}{\mathrm{R}T}\right) \quad [7]$$

where

$$\frac{\gamma\Omega\Gamma D_0}{\mathrm{k}G^m} = \frac{\gamma_{sv}\Omega}{\mathrm{k}}\left(\frac{\Gamma_v D_{v0}}{G^3} + \frac{\Gamma_b \delta_b D_{b0}}{G^4}\right) \quad [8]$$

where $\gamma\Omega\Gamma D_0/\mathrm{k}G^m$ is a symbolic way of representing the terms including surface energy (γ), atomic volume (Ω), Boltzmann's constant (k), the density-dependent parameters Γ, the diffusivity pre-exponential factors (D_0), the thickness of the grain boundaries (δ_b), the grain size (G), and the numerical exponents for grain size (m). Actually, this term is not used to build the master sintering curve, so a detailed knowledge of its value and form is not necessary. In Eq. [7], m is between 3 for volume diffusion and 4 for grain boundary diffusion. In addition, Eq. [7] can be obtained from any couple of diffusion-controlled mechanisms of densification following the procedure explained previously.

It can also be extended to diffusion-controlled densification by solution-reprecipitation during liquid-phase sintering. This densification mechanism can be described using different models.[15] One of them is the contact flattening model proposed by Kingery:[16]

$$\left(\frac{\Delta L}{L_0}\right)^3 = \frac{192\gamma_{lv}\Omega}{\mathrm{k}T}\frac{C_l \delta_l D_{vl}}{G^4}t \quad [9]$$

where $\Delta L/L_0$ is the linear shrinkage, L_0 is the initial value of any linear dimension of the compact, γ_{lv} is the liquid-vapor surface energy, D_{vl} is the diffusivity of the solid in the liquid, δ_l is the width of the liquid film between solid particles, and C_l is the solubility of the solid into the liquid. The original model was proposed for a dihedral angle equal to zero, that is, the solid particles are separated by a continuous liquid layer. However, later simulation work has shown that this equation is still accurate enough for higher dihedral angles and, hence, discontinuous liquid films.[17,18]

For isotropic densification, the linear shrinkage is related to the density variation by the following approximate relationship:

$$\frac{\Delta L}{L_0} = \frac{1}{3}\frac{\Delta\rho}{\rho_0} \quad [10]$$

where Δp is the change in density during sintering and ρ_0 is the original density of the compact. Substituting Eq. [10] in Eq. [9], taking the derivative with time, considering the exponential dependence of the diffusivity with temperature, and rearranging terms, the following expression results:

$$\frac{1}{3\rho}\frac{d\rho}{dt} = \frac{\gamma_{lv}\Omega}{\mathrm{k}}\frac{\Gamma_l C_l \delta_l D_{vl0}}{G^4}\frac{1}{T}\exp\left(-\frac{Q_{vl}}{\mathrm{R}T}\right) \quad [11]$$

where

$$\Gamma_l = \frac{576\rho_0^3}{(\rho-\rho_0)^2\rho} \quad [12]$$

The term D_{vl0} is the pre-exponential factor and Q_{vl} the activation energy for diffusion of the solid atoms through the liquid.

Another model describes densification by solution-reprecipitation as a consequence of the preferential dissolution of small particles and reprecipitation on the largest ones. According to this model, the linear shrinkage can be approximately described by[15]

$$\left(\frac{\Delta L}{L_0}\right)^3 = \frac{48\gamma_{lv}\Omega}{\mathrm{k}T}\frac{C_l D_{vl}}{G^3}t \quad [13]$$

Substituting Eq. [10] in Eq. [13] and operating as before, the following equation results:

$$\frac{1}{3\rho}\frac{d\rho}{dt} = \frac{\gamma_{lv}\Omega}{\mathrm{k}}\frac{\Gamma_l C_l D_{vl0}}{G^3}\frac{1}{T}\exp\left(-\frac{Q_{vl}}{\mathrm{R}T}\right) \quad [14]$$

where

$$\Gamma_l = \frac{144\rho_0^3}{(\rho-\rho_0)^2\rho} \quad [15]$$

Note that Eqs. [11] and [14] display the same dependence of $(1/3\rho)(d\rho/dt)$ with temperature.

Equation [11] or [14] can be combined with either Eq. [3] or [4] to take into account that during liquid-phase sintering the solution-reprecipitation mechanism can be competing with solid-state sintering (by volume or grain boundary diffusion, respectively). Let us say, for example, that a significant contribution of grain boundary diffusion to densification occurs together with the solution-reprecipitation mechanism. We choose Eq. [11] to describe this, although an equivalent result is obtained with Eq. [14]. In this case, adding Eq. [11] to [4] leads to

$$\frac{1}{3\rho}\frac{d\rho}{dt} = \frac{\Omega}{kT}\left[\frac{\gamma_{lv}\Gamma_l C_l \delta_l D_{vl0}}{G^4}\exp\left(-\frac{Q_{vl}}{RT}\right) + \frac{\gamma_{sv}\Gamma_b \delta_b D_{b0}}{G^4}\exp\left(-\frac{Q_b}{RT}\right)\right] \quad [16]$$

This expression is comparable to Eq. [2], so following the same steps as previously discussed, Eq. [7] is attained, where now

$$\frac{\gamma\Omega\Gamma D_0}{kG^m} = \frac{\Omega}{k}\left(\frac{\gamma_{lv}\Gamma_l C_l \delta_l D_{vl0}}{G^4} + \frac{\gamma_{sv}\Gamma_b \delta_b D_{b0}}{G^4}\right) \quad [17]$$

In this case, the term $\gamma\Omega\Gamma D_0/kG^m$ will include also the solubility of the main component into the liquid (C_l), but as mentioned previously, no detailed knowledge of this term is necessary to build a master sintering curve. However, it is important to keep in mind that the apparent activation energy for sintering (Q) will have a value between the activation energies for both competing diffusion processes, that is, Q_{vl} and Q_b in the present example. Obviously, the same conclusion is reached if Eq. [11] is replaced by Eq. [14].

Equation [7] is a very general sintering equation. Provided that the apparent activation energy for sintering (Q), obtained from experimental data, is a constant in the temperature range of interest, it can be used to simulate the sintering process using the concept of the MSC.[9] The MSC is a direct consequence of this model with the assumption that grain growth can be described as a function of density.[9] Equation [1] is rearranged to bring all of the constants and material parameters with slight modification into a single density-dependent parameter, $\Pi(\rho)$, except for the terms related to temperature:

$$\Pi(\rho) \equiv \frac{kr_{ref}}{\gamma\Omega D_0}\exp\left(\frac{Q}{RT_{ref}}\right)\int_{\rho_o}^{\rho}\frac{G^m}{3\rho\Gamma}d\rho \quad [18]$$

Integration is from the initial or green density to the target final density. The remaining terms lead to a parameter that is equivalent to the thermal work performed in reaching the density. This parameter Θ with slight modification is termed the work of sintering:

$$\Theta(t,T) \equiv \int_{t_0}^{t}\frac{r_{ref}}{T}\exp\left[-\frac{Q}{R}\left(\frac{1}{T}-\frac{1}{T_{ref}}\right)\right]dt \quad [19]$$

where r_{ref} is a reference heating rate for the dimensionless Θ parameter and T_{ref} is a reference temperature. In this study, r_{ref} is 10 °C/min and T_{ref} is 1500 °C.

The two terms represented by Eqs. [18] and [19] can be related to each other experimentally when the geometric parameters of microstructure are independent of the thermal sintering path. As a consequence, the MSC can be applied only to powder compacts made from the same powder and by the same green-body processing. Another assumption is that microstructural evolution (both grain size and geometry) is dependent only on density for any given powder and green body.[9]

Note that the work of sintering depends on the time-temperature pathway and contains one activation energy for each step during the sintering process. As explained previously, while the dominant densification mechanism is volume or grain boundary diffusion, most materials densify through a mixture of densification mechanisms, each with changing roles during heating and as the microstructure changes. Because of these mixed events and their complex dependence on temperature, surface area, grain size, and its curvature, the apparent activation energy used in Eq. [19] often does not match a handbook diffusional parameter. Other factors that sometimes modify the kinetics of sintering and its apparent activation energy are small changes in composition, impurities, and the sintering atmosphere. That is why the apparent activation energy is found in this work by a root-mean-square fitting of experimental data with a master sintering curve. This fitting is performed through iteration with the criteria of minimizing the mean residual value.

A sigmoid function provides a good fit between the densification parameter Ψ with range of $\rho_0 < \rho < 1$ and the natural logarithm of the work of sintering, $\ln\Theta$.[19,20] The sigmoid equation used to define the MSC is

$$\Psi = \frac{\rho-\rho_0}{1-\rho_0} = \frac{1}{1+\exp\left[-\frac{\ln\Theta - a}{b}\right]} \quad [20]$$

where ρ_0 is the relative density at the start of the sintering experiment, and a and b are constants defining the curve. An alternative form of Eq. [20] is

$$\Phi \equiv \frac{\rho-\rho_0}{1-\rho} = \frac{\rho-\rho_0}{\theta} = \left(\frac{\Theta}{\Theta_{ref}}\right)^n \quad [21]$$

or

$$\ln\Phi = \ln\left[\frac{\rho-\rho_0}{1-\rho}\right] = n\ln\left(\frac{\Theta}{\Theta_{ref}}\right) = n(\ln\Theta - \ln\Theta_{ref}) \quad [22]$$

with $\ln\Theta_{ref} = a$ and $n = 1/b$. In Eqs. [21] and [22], Φ is the densification ratio with the range of $\rho_0 < \rho < 1$, which is defined as the ratio of density difference between the current density and the initial density to the current porosity θ; n is a slope, power-law exponent, or densification function, which defines the rate of increment of $\ln\Phi$ during the sintering process; and $\ln\Theta_{ref}$ is the natural logarithm of

the work of sintering ln Θ at $\rho = (\rho_0 + 1) / 2$, which is the midpoint of densification or densification to parameter Ψ of 0.5. Note that the relationship between Ψ and Φ is $1/\Psi = 1 + 1/\Phi$. Furthermore, the generalized power-law exponent is defined as

$$n \equiv \frac{d \ln \Phi}{d \ln \Theta} \quad [23]$$

which will be used for constructing multiphase MSCs later in this article.

III. EXPERIMENTAL PROCEDURES

A. *Powder and Sample Preparation*

The characteristics of the as-received W, Ni, and Fe powders selected for this study are given in Table I. The tungsten powder used in the mixture was rod milled to deagglomerate the as-received powder. The rod milling operation was performed dry for 1 hour in a 2000 cm^3 capacity plastic jar at 90 rpm using greater than 95 pct pure tungsten rods with 10-mm diameter and 180-mm length. The weight ratio of rods to powder was 10:1. The milling jar was evacuated, argon back filled, and tape sealed in order to prevent oxidation.

Elemental W, Ni, and Fe powders were weighted accurately to make up the desired compositions. The weighed powders were subsequently placed in a 500 cm^3 capacity plastic jar and mixed in a Turbula mixer (T2C, Glen Mills, Clifton, NJ) for 30 minutes. The homogenously mixed powders were compacted uniaxially into cylinders of 12.7 mm in diameter and 10.0 mm in height using a Carver press at a pressure of 175 MPa. The green densities of all samples for both dilatometry and quenching were 60 pct of theoretical.

B. *Dilatometry Test*

A dilatometer was employed for *in-situ* measurement of shrinkage, shrinkage rate, and the temperature at which phase changes occur. Dilatometry experiments were conducted on 83W, 88W, and 93W with the balance being Ni and Fe in the ratio of 7:3 at heating rates of 2 °C/min, 5 °C/min, and 10 °C/min. The experiments were performed using a vertical push rod dilatometer in hydrogen (ANTER UNITHERM* model 1161) with three different heating rates both in solid-state and liquid-phase sintering to obtain activation energies and to construct MSCs, as shown in Table II. The dilatometer was also used to measure the thermal expansion of each composition during a controlled cooldown at a rate of 20 °C/min from the sintering temperature.

*ANTER UNITHERM is a trademark of Anter Corporation, Pittsburgh, PA.

C. *Quenching Test*

The samples were placed in a molybdenum crucible suspended in the hot zone of a vertical CM furnace with a tungsten wire. The special design of the furnace allowed the sintered compacts to be quenched when the desired temperature and time were reached. The samples were heated at 10 °C/min to 900 °C with a 1-hour hold to reduce oxides on the powders. For solid-state-sintered samples, the temperature was increased to the quench temperature at 5 °C/min for various hold times (0, 30, or 60 minutes). For the liquid-phase-sintered samples, the temperature was increased 10 °C/min to 1400 °C, then 5 °C/min to the quench temperature. Sintering was performed in a dry H_2 atmosphere. The entire crucible was quenched in water to obtain the instantaneous microstructure when the target temperature and time were reached.

Table I. Powder Characteristics and Tungsten Heavy Alloy Composition

Element	W	Ni	Fe
Vendor	Osram (Towanda, PA)	Novamet (Wyckoff, NJ)	ISP (Wayne, NJ)
Designation	M-37	123	CIP-R1470
Fabrication method	oxide reduction	carbonyl process	carbonyl process
Powder properties			
*D*10 (μm)	2	3	2
*D*50 (μm)	6	10	6
*D*90 (μm)	10	24	10
apparent density (g/cm^3)	4.1 (21 pct)	2.3 (26 pct)	2.4 (31 pct)
tap density ((g/cm^3)	6.2 (32 pct)	3.3 (37 pct)	4.6 (59 pct)
pycnometer density (g/cm^3)	19.20	8.96	7.89
BET surface area (m^2/g)	0.18	0.60	0.45
83 pct WHA			
wt pct	83.0	11.9	5.1
vol pct	68.5	21.2	10.3
density (g/cm^3)		15.94	
88 pct WHA			
wt pct	88.0	8.4	3.6
vol pct	76.6	15.7	7.7
density (g/cm^3)		16.80	
93 pct WHA			
wt pct	93.0	4.9	2.1
vol pct	85.6	9.7	4.7
density (g/cm^3)		17.76	

Table II. Sinter Cycle for Obtaining Activation Energies and Constructing MSCs

solid state	
cycle I	20 °C to 900 °C, 10 °C/min, no hold 900 °C to 1500 °C, 2 °C/min, 10-min hold 1500 °C to 20 °C, 10 °C/min
cycle II	20 °C to 900 °C, 10 °C/min, no hold 900 °C to 1500 °C, 5 °C/min, 10-min hold 1500 °C to 20 °C, 10 °C/min
cycle III	20 °C to 900 °C, 10 °C/min, no hold 900 °C to 1500 °C, 10 °C/min, 10-min hold 1500 °C to 20 °C, 10 °C/min
liquid state	
cycle I	20 °C to 1455 °C, 15 °C/min, no hold 1455 °C to 1500 °C, 1 °C/min, 10-min hold 1500 °C to 20 °C, 10 °C/min
cycle II	20 °C to 1455 °C, 15 °C/min, no hold 1455 °C to 1500 °C, 2 °C/min, 10-min hold 1500 °C to 20 °C, 10 °C/min
cycle III	20 °C to 1455 °C, 15 °C/min, no hold 1455 °C to 1500 °C, 3 °C/min, 10-min hold 1500 °C to 20 °C, 10 °C/min

The quenched samples were sectioned top to bottom and mounted using epoxy resin under vacuum to fill the porosity and to prevent the smearing of the material into the pores. The polishing procedure involves the use of a 9-μm diamond suspension followed by 6-, 3-, 1-μm diamond suspension on a MD-Dac cloth from Struers (Westlake, OH). A mirrorlike finish was obtained by giving a final polish with a 0.04-μm silica colloidal suspension (OP-S from Struers). The microstructure was imaged using scanning electron microscopy (SEM; TopCon model ABT-32, TopCon, Manchester, United Kingdom). These SEM pictures were used to explain densification behavior in terms of microstructure.

IV. RESULTS

Figure 1(a) shows the relationship between the densification parameter (Ψ) and the work of sintering (Θ) directly plotted from the dilatometry data in the case of the alloy with 93 wt pct of W. For the other compositions, the curves are similar. This is basically the traditional MSC plot used earlier in the literature.[9,20] Figure 1(b) presents one of the modifications proposed in this article, which is substituting the densification parameter (Ψ) with the densification ratio (Φ). This modification makes it easier to identify the three regions of the curve into which it can be divided.

Based on the W-Ni-Fe ternary phase diagram[21] and Figure 1(b), these three regions can be roughly identified as follows: (1) region I, low-temperature or solid-state sintering region ($T < 1400$ °C); (2) region II, intermediate temperature or transition region (1400 °C $\leq T <$ 1455 °C); and (3) region III, high-temperature or liquid-phase sintering region ($T \geq 1455$ °C). Obviously, interdiffusion during heating will shift the onset temperature for each region. The three regions are defined, based on Eq. [22], by the following three equations.

Region I, low-temperature region or solid-state sintering region (<1400 °C):

$$\ln\ \Phi = n(\ln\ \Theta - \ln\ \Theta_{\text{ref}}) \qquad [24]$$

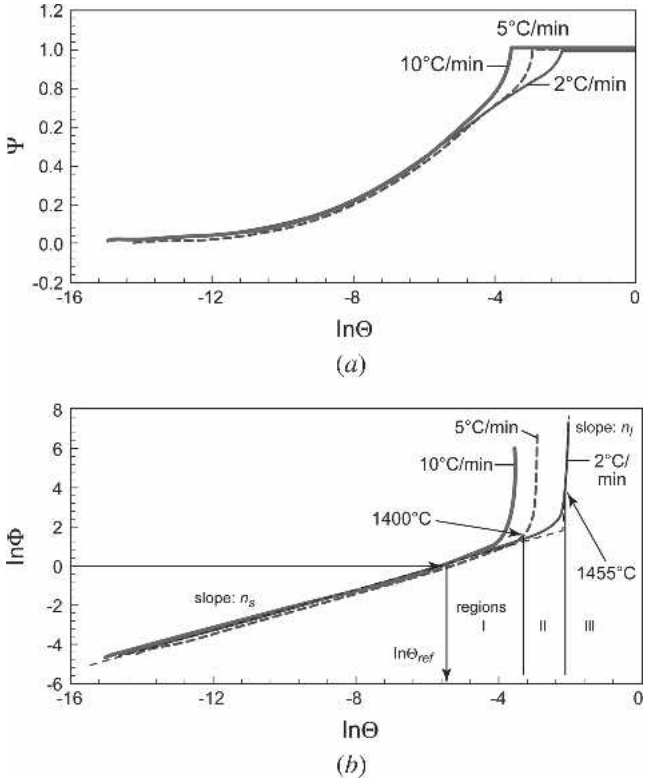

Fig. 1—MSC plots for 93W-4.9Ni-2.1Fe: (*a*) densification parameter plot and (*b*) densification ratio plot.

with $Q = Q_s$ (the activation energy for solid-state sintering) and $n = n_s$ (the densification function for solid-state sintering).

Region II, intermediate temperature or transition region (1400 °C $\leq T <$ 1455 °C):

$$d\ \ln\ \Phi = nd\ \ln\ \Theta \qquad [25]$$

with $Q = Q_{sl}$ (the activation energy of sintering in this region) and $n = n_{sl}$ (densification function in this region). In this study, Q_{sl} is linearly interpolated from Q_s and Q_l on the basis of temperature and n_{sl} is calculated from experimental data using Eq. [23].

Region III, high-temperature or liquid-phase sintering region ($T \geq 1455$ °C):

$$d\ \ln\ \Phi = nd\ \ln\ \Theta \qquad [26]$$

with $Q = Q_l$ (the activation energy for liquid-phase sintering) and $n = n_l$ (the densification function for liquid-phase sintering).

In region I, below the solidus temperature of the alloy, densification can be fully described with Eq. [24] using the same apparent activation energy (Q_s) and densification function parameter (n_s) for every temperature and heating rate. The same is also true for region III, where the additive phase has melted completely. In this region, both parameters (Q_l and n_l) are also independent of the temperature and heating rate, proving that the concept of MSC can be extended to liquid-phase sintering. However, in region II, where the additive phase is melting and alloying progressively, the value of both parameters changes with increasing temperature because the contribution to densification is shifting from solid-state to liquid-phase mechanisms.

Figure 2 shows the microstructural evolution of the material during solid-state sintering. Densification when increasing the temperature is evident in the micrographs. It is also worthy to remark that W grains are rounded with grain growth at higher temperatures, in conformity with a dissolution-precipitation process. Additionally, the pictures show that when the temperature increases, necks develop between W particles, making possible the contribution of W grain boundary diffusion to the densification of the material.

Figure 3 shows the typical microstructure of the material after melting of the additive phase. When the sample reaches 1480 °C, it is completely dense. Additionally, the morphology of the grains is more rounded, as a consequence of the enhanced dissolution-precipitation that occurs when the liquid phase appears. This also originates grain growth by Ostwald ripening, which is evident in the micrographs.

Figure 4(a) shows that the densification function during solid-state sintering, n_s, can be considered as a constant for the entire range of temperature (1000 °C to 1400 °C) where densification occurs with 2 °C/min to 10 °C/min of heating rate. In addition, the densification function, n_s, which is related to the speed of densification, increases slightly during solid-state sintering as the amount of W decreases, as shown in Figure 4(b) and Table III. Like solid-state sintering, the densification function, n_l, increases during liquid-phase sintering as the amount of W decreases.

V. DISCUSSION

Tungsten heavy alloys increase their density by both solid-state and liquid-phase sintering.[2–5] The relative contribution of these mechanisms depends on experimental

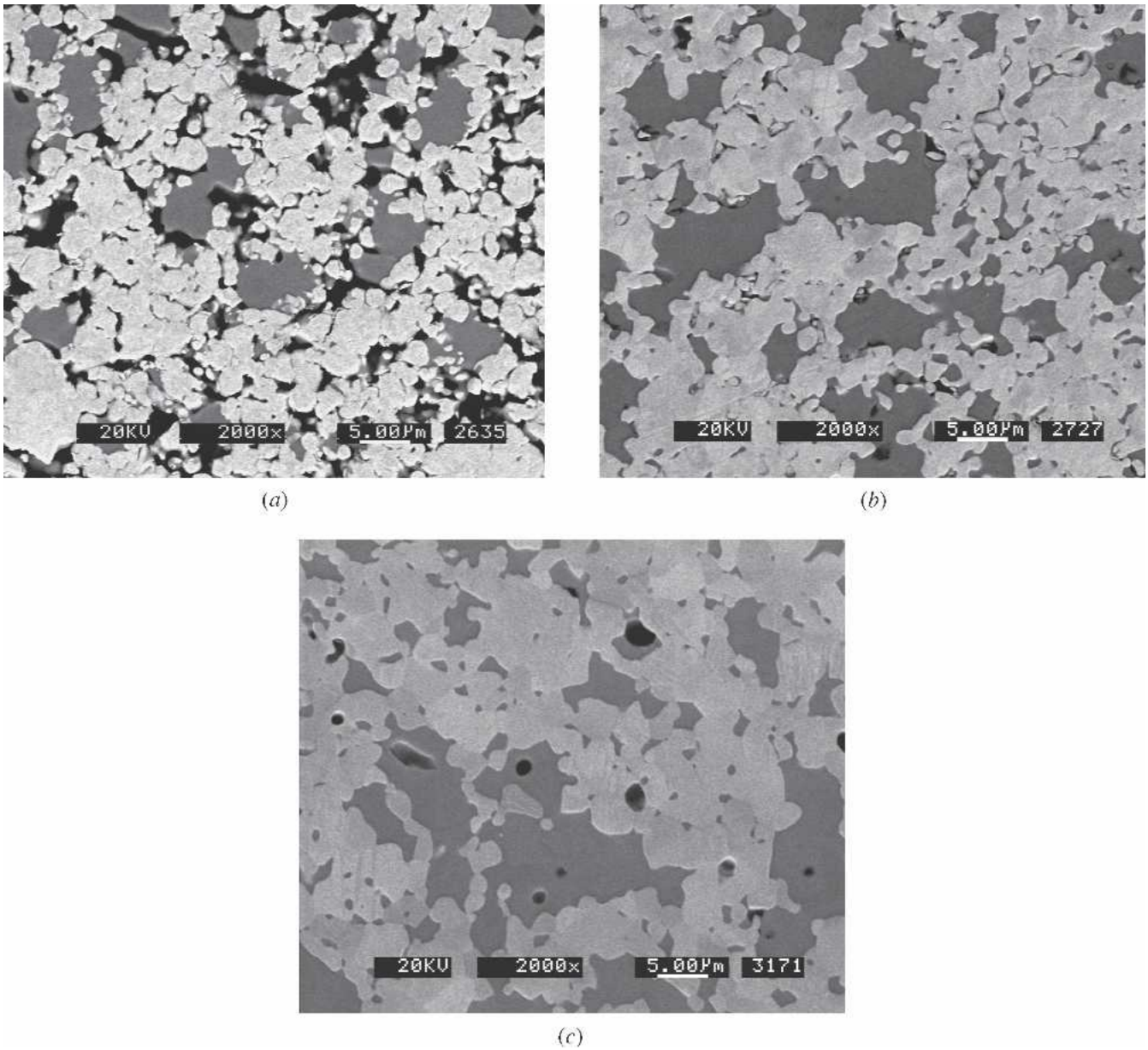

Fig. 2—SEM micrographs of 88W-8.4Ni-3.6Fe during solid-state sintering: (*a*) 1200 °C with no hold, (*b*) 1300 °C with no hold, and (*c*) 1400 °C with no hold.

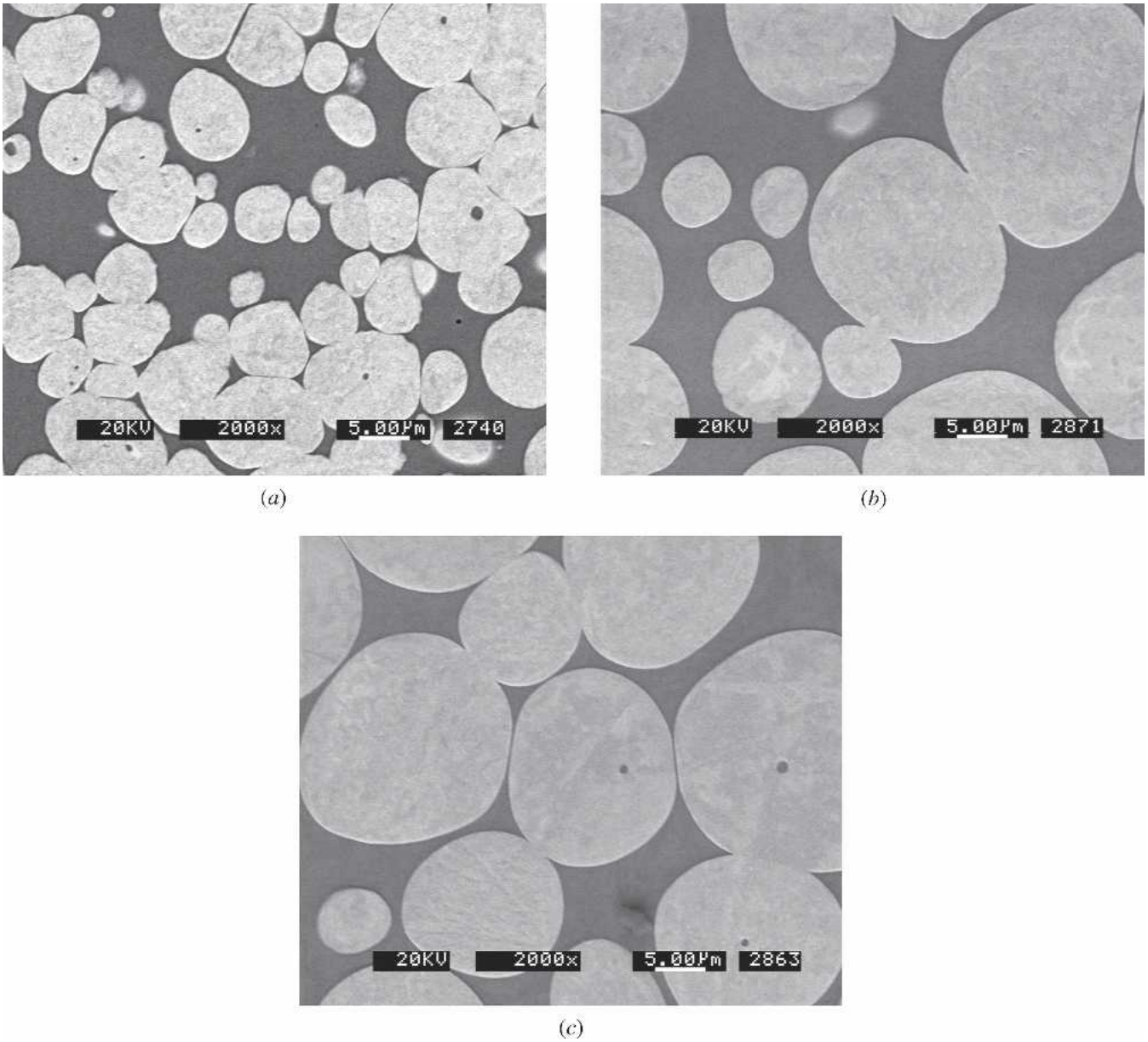

Fig. 3—SEM micrographs of 88W-8.4Ni-3.6Fe during liquid-phase sintering: (*a*) 0 min hold at 1480 °C, (*b*) 30 min hold at 1480 °C, and (*c*) 60 min hold at 1480 °C.

parameters such as the amount of additive phase and its composition, W grain size, and sintering cycle.[3–5,22] Tables IV and V summarize the densification mechanisms that can be active, respectively, during solid-state and liquid-phase sintering for these materials.[2,4,5,8,23–28] When analyzed quantitatively from a kinetic point of view, each one of them can be related to the activation energy of a diffusion process, except for the case of rearrangement.

Approximated values for these activation energies in solid-state sintering are also included in Table IV.[26] As activation energies for the ternary system W-Ni-Fe could not be found in the literature, values belonging to the binary systems W-Ni and W-Fe are presented. In the case of liquid-phase sintering, the activation energy for W diffusion into either molten Ni or Fe is not available. However, a W diffusion coefficient in liquid Ni of $(2.4 \pm 0.2)\cdot 10^{-9}$ m^2/s, with an additional systematic uncertainty of $\pm 0.5\cdot 10^{-9}$ m^2/s due to instrumental and surface effects, has been recently reported.[29] This value is the average of three measurements between 1482 °C and 1688 °C, that is, in a temperature range just above the melting point of Ni (1453 °C). The self-diffusion coefficient of liquid Ni has been calculated theoretically[30,31] in this temperature range giving values of $3.84\cdot 10^{-9}$ to $4.61\cdot 10^{-9}$ m^2/s at 1500 °C and $5.88\cdot 10^{-9}$ to $6.76\cdot 10^{-9}$ m^2/s at 1650 °C. An experimental measurement at 1500 °C gave $4.0\cdot 10^{-9}$ m^2/s.[32] These data are between 1.6 and 2.8 times higher than the experimental value for W diffusion in liquid Ni, but they are of the same order of magnitude.

Thus, considering the lack of data for the activation energy of W diffusion in the liquid Ni-Fe-W solution existing in region III, a convenient estimate could be the activation

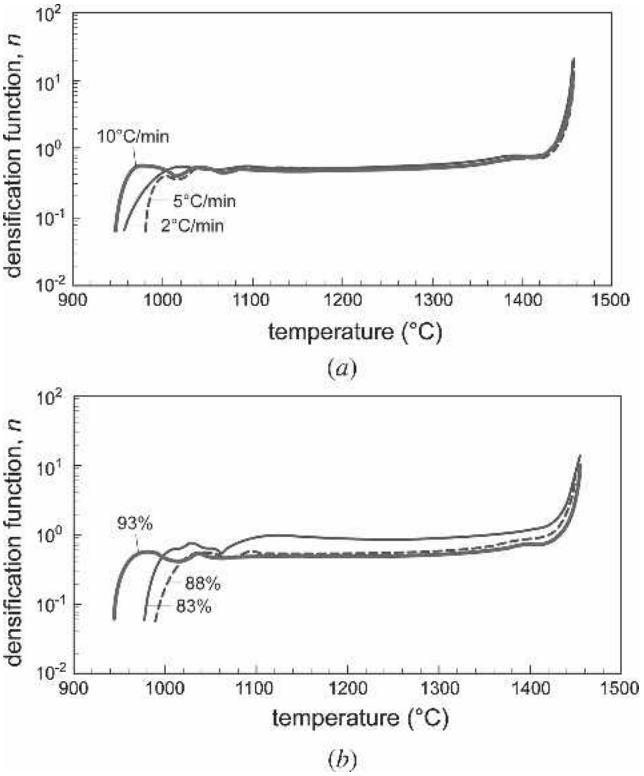

Fig. 4—Densification function plots based on MSC: (*a*) densification function plot for 93 pct WHA and (*b*) densification function plot with various alloy systems.

Table III. Summary of MSC Parameters and Thermal Expansion Coefficients

Material Parameters	83 pct WHA	88 pct WHA	93 pct WHA
$\ln \Theta_{ref}$	−4.12	−5.41	−5.47
n_s	0.756	0.606	0.513
n_l	19.9	18.0	14.2
Thermal expansion coefficient (10^{-6} K^{-1})	11.23	9.27	7.83

Note that thermal expansion coefficient values are $4.6 \cdot 10^{-6}$ K^{-1} for W, $13.3 \cdot 10^{-6}$ K^{-1} for Ni, and $12.3 \cdot 10^{-6}$ K^{-1} for Fe.[7]

energy for self-diffusion in Ni. Although these activation energies are surely different, it is expected that they will be similar in magnitude and much lower than the values presented in Table IV for solid-state diffusion processes. To illustrate this last assertion, the ranges of activation energies for self-diffusion and impurity diffusion of several transition metals in liquid Fe[27] are also included in Table V, along with the data for self-diffusion in liquid Ni.[28] Comparing the activation energies in both tables, the lower magnitude of activation energies for diffusion in liquid metals is evident. This is enough for the subsequent discussion about sintering mechanisms developed in this article.

Table VI shows the apparent activation energies obtained from the construction of the MSC from dilatometry data when the mean square residuals are minimized. These data will be compared with values in Tables IV and V in subsequent sections in order to obtain some knowledge about the most significant densification mechanisms occurring during sintering. According to a main hypothesis underlying the building of a MSC,[9] a constant value of the apparent activation energy means that the dominant densification mechanism remains the same in the specific range of times and temperatures where sintering was done. However, as mentioned previously, the densification of real systems usually takes place by a combination of mechanisms rather than by only one. Even in this case, a constant value will result if the proportional contribution of each mechanism does not change.

A. *Solid-State Sintering*

When heating to 1400 °C, several mechanisms can contribute simultaneously to the shrinkage of the sample. The activation energy associated with these processes is a measure of the relative rate at which they occur. The higher the activation energy is, the lower the kinetics of the related densification process. According to the data in Table IV, the lower activation energies correspond to grain boundary diffusion (97 to 234 kJ/mol) and lattice diffusion (254 to 306 kJ/mol) into the additive phase. Consequently, the most important events at low temperatures should be the sintering of the additive Ni-Fe particles by these mechanisms and their interdiffusion to form a face-centered cubic (fcc) solid solution. The literature does not usually report that sintering of the additive phase contributes to the global densification of the compact in the system W-Ni-Fe, probably because contacts between W particles hinder the shrinkage. However, the results of Lee and Moon[24] for the W-Ni system suggest that a moderate contribution takes place, particularly for the samples with a higher amount of additive phase.

The shrinkage caused by additive phase sintering has been better described in the W-Cu system, particularly with nanocomposite powders obtained by either hydrogen coreduction of W-Cu oxide powder mixtures or mechanical alloying.[25,33–35] Probably the description holds also for the W-Ni-Fe system. It starts when the solid additive phase spreads by diffusion or viscous flow on the surface of W particles.[25,33,36] As a result, the additive phase fills the smaller pores between W particles forming dense W-additive phase aggregates. Next, these aggregates sinter within them growing necks of additive phase. The process has also been termed rearrangement in the solid state.[33] The spreading of the additive phase and the filling of small porosity is evident when comparing the microstructures at 1200 °C and 1300 °C (Figures 2(a) and (b)).

The dissolution of the W particles into the Ni-Fe based fcc solution also promotes densification. The rate at which this phenomenon occurs is controlled by the activation energy of the diffusion coefficient of W in the Ni-Fe fcc phase (around 268 to 306 kJ/mol). The total shrinkage by these mechanisms can be calculated using the model proposed by Savitskii:[23]

$$\frac{\rho_f - \rho_0}{\rho_0} = \frac{C_{ad} C_s}{1 - C_{ad} - C_s} \qquad [27]$$

Table IV. Densification Mechanism for Solid-state Sintering of W-Ni-Fe Alloys; Activation Energies and Temperature Range of Validity for the Corresponding Diffusion Coefficients[26]

Mechanism	Temperature Range and Activation Energy	
	T (°C)	Q (kJ/mol)
Lattice diffusion of the additive	675 to 1404	Q_v^{Ni}: 279 to 294
	950 to 1393	$Q_v^{Fe(\gamma)}$: 270 to 311
	635 to 1426	$Q_v^{Fe-70Ni}$: 254 to 306*
Lattice diffusion of the W	1432 to 3228	Q_v^{W}: 526 to 666
Grain boundary diffusion of the additive	368 to 1100	Q_b^{Ni}: 115 to 234
	918 to 1200	$Q_b^{Fe(\gamma)}$: 97 to 181
Grain boundary diffusion of the W	1397 to 2150	Q_b^{W}: 379 to 385
Dissolution of the main component into the additive	1000 to 1316	Q_v^{Ni-W}: 295 to 306**
	912 to 1485	$Q_v^{Fe(\gamma)-W}$: 268†
Dissolution precipitation through the additive (diffusion controlled)	1000 to 1316	Q_v^{Ni-W}: 295 to 306**
	912 to 1485	$Q_v^{Fe(\gamma)-W}$: 268†

*Chemical diffusion coefficient for Fe-70Ni (wt pct).
**Chemical diffusion coefficient for Ni-(19.1 to 25.8 wt pct) W.
†Chemical diffusion coefficient for Fe(γ)-(0 to 9.0 wt pct) W.

Table V. Additional Densification Mechanisms for Liquid-Phase Sintering of W-Ni-Fe Alloys; Activation Energies for Self-Diffusion in Liquid Fe ($Q_{Fe}^{Fe(l)}$), Impurity Diffusion of Some Transition Metals in Liquid Iron ($Q_M^{Fe(l)}$), and Self-Diffusion in liquid Ni ($Q_{Ni}^{Ni(l)}$) Near the Melting Point

Mechanism	Q (kJ/mol)
Rearrangement	—
Dissolution of the main component into the liquid and dissolution-precipitation through the liquid (diffusion controlled)	$Q_{Fe}^{Fe(l)}$: 51.1 to 65.7*
	$Q_M^{Fe(l)}$: 16.3 to 47.7*
	$Q_{Ni}^{Ni(l)}$: 35.1 to 78.9**

Note that these activation energies are relevant when discussing liquid-phase sintering mechanisms involving diffusion through the liquid in W-Ni-Fe heavy alloys. No activation energy can be related with densification by rearrangement.
*Experiment.[27]
**Calculated from theoretical models.[28]

where ρ_f is the density after dissolution, ρ_0 is the green density, C_{ad} is the volume concentration of additive phase, and C_s is the solubility (volume fraction) of W in the Ni-Fe based fcc solid solution. This ideal model supposes that dissolution takes places evenly on the entire surface of W particles, so that they do not change their shape. In real compacts, this is not fulfilled, and the actual densification is lower than predicted by the model. Table VII shows the value of density, densification parameter, and densification ratio after dissolution of W into the fcc additive phase calculated using the model of Savitskii for the materials used in this work. The values of solubility (C_s) were obtained from the W-Ni-Fe ternary phase diagram.[21] These values indicate only moderate densification due to this effect.

According to the previous explanations, only limited densification is expected by either the sintering of the additive phase or by the dissolution of W into it, so other mechanisms must be active. The next one to be considered in ascending order of activation energies is dissolution-precipitation of W through the additive phase (295 to 306 kJ/mol). This mechanism is active once the fcc additive phase is saturated with W. Krock[2] reported that the solid-state sintering of W-Ni-Fe takes place in this way, measuring an apparent activation energy of 383 kJ/mol. This mechanism has also been mentioned in relation to the Ni-activated sintering of W and Mo.[13,24]

However, other authors describe the activated sintering process as an enhanced W grain boundary diffusion process[37] rather than as a diffusion process through the additive phase. In this case, the associated activation energy should be lower than the value given in Table III for pure W (379 to 385 kJ/mol), but a more precise value could not be found. Regardless of whether the process is activated, a significant contribution of W grain boundary diffusion mechanism to densification must always be considered. The occurrence of this contribution has been observed during sintering of W-Cu alloys[5,25] and pure W.[14] On the other hand, W lattice diffusion is not an active densification mechanism in this range of temperatures because of the high activation energy (526 to 666 kJ/mol).

The values of apparent activation energies obtained from the MSC analysis in region I (Table VI) are between the activation energy for lattice diffusion of W in the fcc additive phase (295 to 306 kJ/mol) and W grain boundary diffusion (379 to 385 kJ/mol). Consequently, most of the densification is expected to occur by a combination of both. The increase of the activation energy with the W content is also coherent with this conclusion, as it reflects a higher contribution of the W grain boundary diffusion mechanism. Further, this result correlates with the decrease in the densification function, n_s, as the W content increases, as shown in Table III. By quantifying and interpolating based on the MSC parameters, Q_s, n_s, and ln Θ_{ref}, given in Table III, densification behavior can be predicted during solid-state sintering for 83 to 93 WHA systems.

Table VI. Activation Energies for Solid-State and Liquid-Phase Sintering Used in Constructing MSC

	Region I (Solid)		Region III (Liquid)	
Phase	Q_s (kJ/mol)	Mean Residual	Q_l (kJ/mol)	Mean Residual
83 pct WHA	262	22.5 pct	101	29.3 pct
88 pct WHA	367	17.7 pct	127	25.9 pct
93 pct WHA	387	15.9 pct	136	28.5 pct

Table VII. Density (ρ_f), Densification Parameter (Ψ), and Densification Ratio (Φ) as a Function of Temperature after Dissolution of W into the Fcc Additive Phase Calculated According to the Savitskii Model[23]

Alloy	C_{ad} (Vol Pct)	T (°C)	C_s (Vol Pct)	ρ_f (Pct)	Ψ	ln Φ
83 pct WHA	31.5	1100	10.3	63.4	0.084	−2.39
		1250	11.8	63.9	0.099	−2.21
		1400	13.8	64.8	0.119	−2.00
88 pct WHA	23.4	1100	10.3	62.2	0.055	−2.85
		1250	11.8	62.6	0.064	−2.68
		1400	13.8	63.1	0.077	−2.48
93 pct WHA	14.4	1100	10.3	61.2	0.030	−3.48
		1250	11.8	61.4	0.035	−3.32
		1400	13.8	61.7	0.042	−3.13

Note that green density is 60 pct.

B. *Transient Zone*

Region II in Figure 1(b) corresponds roughly with the temperature interval in which Ni-Fe-W fcc solid solution (additive phase) melts, according to the phase diagram.[21] During this transition period between 1400 °C and 1450 °C, the amount of liquid in the system increases continuously with temperature from zero until about 14 vol pct for 93 wt pct W alloy, 25 vol pct for 88 wt pct W alloy, and 36 vol pct for 83 wt pct W alloy. Consequently, there are solid and liquid densification mechanisms active at the same time. Moreover, liquid-phase sintering becomes more and more important compared with solid-state sintering with increasing temperature, so it is not possible to describe the densification using only one constant value for the activation energy (Q) and for the densification function parameter (n). Instead, the value of activation energy has been interpolated linearly with temperature between the end values corresponding to solid-state (Q_s) and liquid-phase sintering (Q_l). Then, the densification function parameter value is calculated directly from the experimental data using Eq. [23].

The transitory liquid being generated in this region is able to penetrate through the W particle necks and to separate grains in a few minutes.[7] This might make possible the densification by rearrangement, which is also a very fast process.[8] The amount of densification by rearrangement will vary with the solid volume fraction of the material and the heating rate. In the present case, the density of the compacts at the beginning of region II is already high. For example, it is about 84 pct for every alloy when the heating rate is 10 °C/min. This density corresponds to W volume fractions of 0.71 for 93 wt pct W alloy, 0.62 for 88 wt pct W alloy, and 0.52 for 83 wt pct W alloy. The solid volume fraction corresponding to a random dense packing of monosized spheres is 0.610-0.667.[38] As a result, it is not expected that rearrangement will contribute any significant densification in the case of 93 wt pct W; it will contribute slightly in the case of 88 wt pct W; and a complete densification by rearrangement, corresponding to a 0.61 solid volume fraction, probably will occur with the 83 wt pct W alloy. When the heating rate is reduced from 10 °C/min to 2 °C/min, the density at the beginning of region II is higher, so the rearrangement contribution to densification is smaller.

C. *Liquid-Phase Sintering*

The remaining densification up to 100 pct relative density mainly occurs by dissolution-precipitation of the W particles through the Ni-Fe-W liquid phase, as this is the active process with the lowest activation energy (about 24.3 to 78.9 kJ/mol according to the data in Table V). Thus, the experimental values determined for the activation energies are much lower in Region III (liquid-phase sintering) than in region I (solid-state sintering), as shown in Table IV.

A comparison of Figure 2 with Figure 3 shows that the number of W particle necks after liquid formation is smaller than in solid-state sintering, demonstrating that most of them were broken during the generation of the liquid in region II. This suggests also a reduction in the contribution of the grain boundary diffusion mechanisms in region III compared with region I. However, the experimental values for region III in Table VI are higher than the data of Table V, and, what is more significant, they increase slightly with the amount of W in the alloy. This result correlates with the decrease in the densification function, n_s, as the W content increases, as shown in Table III, and indicates that a minor contribution to sintering of W grain boundary diffusion simultaneously takes place. Densification behavior can be predicted for 83 to 93 WHA systems

by quantifying and interpolating based on the MSC parameters, Q_l and n_l.

D. *Master Sintering Surface*

In this study, densification behavior was systematically and completely quantified during both solid-state sintering and liquid-phase sintering for 83, 88, and 93 WHA systems by using the MSC approach and sigmoid function model, as shown in Tables III and VI . All parameters show logical trends as the W amount increases. The sigmoid model based on the MSC has good agreement with experimental data within 1.0 pct relative error. Table III shows that densification occurs faster in the lower W system (higher value of "n") and thermal expansion coefficients are well placed between the values of W and the values of Ni and Fe. Additionally, as discussed previously, the activation energies obtained from MSC analysis are coherent with densification mechanisms proposed in the literature. These results provide strong evidence that the MSC is a good tool for analyzing and quantifying densification behavior for multiphase sintering systems.

Figure 5 shows the master sintering surface (MSS), which is a series of MSCs with varying tungsten amounts. From this plot, the density can be predicted for any given 83 to 93 wt pct WHA system and sintering cycle. Such MSSs are very useful for determining optimum combinations of material compositions and sintering cycles.

VI. CONCLUSIONS

Substituting the densification ratio (Φ) for the densification parameter (Ψ) in MSC theory helps identify regions where shrinkage is taking place by the same combination of sintering mechanisms. This identification enables extension of the MSC concept to sintering processes in which a change of phase occurs, such as sintering of WHAs. Apparent activation energies for sintering in each identified region of the multiphase MSC can be obtained. Comparing these activation energies with experimental values for diffusion or other mass-transport phenomena enables identification of the dominant densification mechanisms in each region. For sintering of WHAs at temperatures up to 1400 °C, densification occurs through a combination of both lattice diffusion of W in the additive phase and W grain boundary diffusion. At temperatures above 1455 °C, dissolution-precipitation of the W particles through the Ni-Fe-W liquid phase is the dominant densification mechanism. Between 1400 °C and 1455 °C, the MSC shows a transition region in which a combination of the solid-state and liquid-phase mechanisms is active. The densification function, n, increases during both solid-state and liquid-phase sintering as the amount of W decreases. Densification behavior can be predicted for 83 to 93 wt pct W heavy alloy by quantifying and interpolating the MSC parameters to construct a master sintering surface.

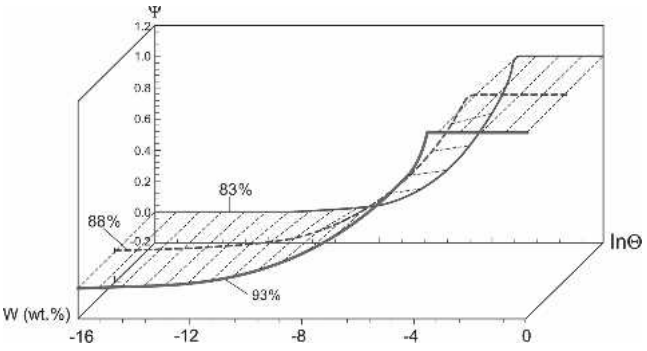

Fig. 5—Master sintering surface with various tungsten weight percentages.

ACKNOWLEDGMENTS

This research was supported by the National Aeronautics and Space Administration under Grant No. NAG8-1452 with Mike Purvey as Project Manager and Witold Palosz as Project Scientist. The stay of J. M. Martin at CISP is partially supported by the Departamento de Educación, Universidades e Investigación of the Basque Government. Special thanks go to Kristina Cowan for her help with the dilatometry and to Lou Campbell for his help with the metallography.

REFERENCES

1. A. Belhadjhamida and R.M. German: in *Tungsten and Tungsten Alloys*, A. Crowson and E.S. Chen, eds., TMS, Warrendale, PA, 1991, pp. 21-26.
2. R.H. Krock: *Proc. American Society for Testing and Materials*, ASTM, Philadelphia, PA, 1964, vol. 64, pp. 669-79.
3. S. Farooq, A. Bose, and R.M. German: in *Progress in Powder Metallurgy*, C.L. Freeby and H. Hjort, eds., MPIF-APMI, Princeton, NJ, 1987, vol. 43, pp. 65-77.
4. J.K. Park, S.J.L. Kang, K.Y. Eun, and D.N. Yoon: *Metall. Trans. A*, 1989, vol. 20A, pp. 837-45.
5. J.L. Johnson and R.M. German: *Metall. Mater. Trans. B*, 1996, vol. 27B, pp. 901-09.
6. J.L. Johnson and R.M. German: *Metall. Mater. Trans. A*, 1996, vol. 27A, pp. 441-50.
7. R.M. German: *Sintering Theory and Practice*, John Wiley & Sons, New York, NY, 1996, pp. 67-141, 225-312.
8. J. Liu and R.M. German: *Metall. Mater. Trans. A*, 2001, vol. 32A, pp. 3125-31.
9. H. Su and D.L. Johnson: *J. Am. Ceram. Soc.*, 1996, vol. 79, pp. 3211-17.
10. G.C. Kuczynski: *Trans. Am. Inst. Mining Met. Eng.*, 1949, vol. 185 (2), pp. 169-78.
11. H. Su and D.L. Johnson: *J. Am. Ceram. Soc.*, 1996, vol. 79 (12), pp. 3199-210.
12. R.M. Cannon and R.L. Coble: in *Deformation of Ceramic Materials*, R.C. Bradt and R.E. Tressler, eds., Plenum Press, New York, NY, 1975, pp. 81-100.
13. J.T. Smith: *J. Appl. Phys.*, 1965, vol. 36 (2), pp. 595-98.
14. T. Vasilos and J.T. Smith: *J. Appl. Phys.*, 1964, vol. 35 (1), pp. 215-17.
15. R.M. German: *Liquid Phase Sintering*, Plenum Press, New York, NY, 1985, pp. 101-21.
16. W.D. Kingery: *J. Appl. Phys.*, 1959, vol. 30 (3), pp. 301-06.
17. G.H. Gessinger and H.F. Fischmeister: *J. Less-Common Met.*, 1972, vol. 27, pp. 129-41.
18. G.H. Gessinger, H.F. Fischmeister, and H.L. Lukas: *Acta Metall.*, 1973, vol. 21, pp. 715-24.
19. M.-H. Teng, Y.-C. Lai, and Y.-T. Chen: *West. Pac. Earth Sci.*, 2002, vol. 2 (2), pp. 171-80.
20. D.C. Blaine, J.D. Gurosik, S.J. Park, D. Heaney, and R.M. German: *Metall. Mater. Trans. A*, 2006, vol. 37A, pp. 715-20.
21. P. Villars, A. Prince, and H. Okamoto: *Handbook of Ternary Alloy Phase Diagrams*, ASM INTERNATIONAL, Materials Park, OH, 1995, vol. 8.
22. S.H. Hong and H.J. Ryu: *Mater. Sci. Eng., A*, 2003, vol. 344 (1–2), pp. 253-60.

23. A.P. Savitskii: *Liquid Phase Sintering of the Systems with Interacting Components*, Russian Academy of Sciences, Siberian Branch, Institute of Strength Physics and Materials Science, Tomsk, 1993, pp. 97-105.
24. J.S. Lee and I.H. Moon: *Scripta Metall.*, 1987, vol. 21, pp. 1175-78.
25. J.S. Lee and T.H. Kim: *Nanostruct. Mater.*, 1995, vol. 6, pp. 691-94.
26. H. Mehrer: *Diffusion in Solid Metals and Alloys*, Landolt-Börnstein Numerical Data and Functional Relationships, New Series, Group III, Spring-Verlag, Berlin, Germany, 1990, vol. 26, pp. 32-84, 297-371, 630-716.
27. A.R. Wilson: *Metall. Rev.*, 1965, vol. 10 (40), pp. 381-590.
28. F.J. Cherne and M.I. Baskes: *Phys. Rev. B: Condens. Matter Mater. Phys.*, 2002, vol. 65, p. 024209.
29. J.P. Leonard, T.J. Renk, M.O. Thompson, and M.J. Aziz: *Metall. Mater. Trans. A*, 2004, vol. 35A, pp. 2803-07.
30. I. Yokoyama and T. Arai: *J. Non-Cryst. Solids*, 2001, vols. 293–295, pp. 806-11.
31. I. Yokoyama: *Physica B*, 1999, vol. 271, pp. 230-34.
32. C. Guminski: *Liquid Metal Systems*, H.U. Borgstedt and G. Frees, eds., Plenum Press, New York, NY, 1995, pp. 345-56.
33. F. Dore, C.L. Martin, and C.H. Allibert: *Mater. Sci. Eng., A*, 2004, vol. 383, pp. 390-98.
34. F.A. da Costa, A.G.P. da Silva, and U.U. Gomes: *Powder Technol.*, 2003, vol. 134, pp. 123-32.
35. D.G. Kim, G.S. Kim, S.T. Oh, and Y.D. Kim: *Mater. Lett.*, 2004, vol. 58, pp. 578-81.
36. H.R. de Macedo, A.G.P. da Silva, and D.M.A. de Melo: *Mater. Lett.*, 2003, vol. 57, pp. 3924-32.
37. N.M. Hwang, Y.J. Park, D.Y. Kim, and D.Y. Yoon: *Scripta Mater.*, 2000, vol. 42, pp. 421-25.
38. R.M. German: *Particle Packing Characteristics*, MPIF, Princeton, NJ, 1989 pp. 106-09.